MDPI

Article

Disaster-Caused Power Outage Detection at Night Using VIIRS DNB Images

Haodong Cui [1], Shi Qiu [1,2,*], Yicheng Wang [3], Yu Zhang [1], Zhaoyan Liu [1], Kirsi Karila [4], Jianxin Jia [4] and Yuwei Chen [4]

1 Key Laboratory of Quantitative Remote Sensing Information Technology, Aerospace Information Research Institute, Chinese Academy of Sciences, Beijing 100094, China
2 State Key Laboratory of Applied Optics (SKLAO), Changchun Institute of Optics, Fine Mechanics and Physics (CIOMP), Chinese Academy of Sciences, Changchun 130033, China
3 Advanced Laser Technology Laboratory of Anhui Province, Hefei 230009, China
4 Department of Remote Sensing and Photogrammetry, Finnish Geospatial Research Institute, FI-00521 Helsinki, Finland
* Correspondence: qiushi@aircas.ac.cn

Abstract: Rapid disaster assessment is critical for public security and rescue. As a secondary disaster of large-scale meteorological disasters, power outages cause severe outcomes and thus need to be monitored efficiently and without being costly. Power outage detection from space-borne remote sensing imagery offers a broader coverage and is more temporally sensitive than ground-based surveys are. However, it is challenging to determine the affected area accurately and quantitatively evaluate its severity. Therefore, a new method is proposed to solve the above problems by building a power outage detection model (PODM) and drawing a power outage spatial distribution map (POSDM). This paper takes the winter storm Uri, of 2021, as the meteorological disaster background and Harris County, Texas, which was seriously affected, as the research object. The proposed method utilises the cloud-free VIIRS DNB nadir and close nadir images (<60 degrees) collected during the 3 months before and 15 days after Uri. The core idea beneath the proposed method is to compare the radiance difference in the affected area before and after the disaster, and a large difference in radiance indicates the happening of power outages. The raw radiance of night light measurement is first corrected to remove lunar and atmospheric effects to improve accuracy. Then, the maximum and minimum pixels in the target area of the image are considered outliers and iteratively eliminated until the standard deviation change before and after elimination is less than 1% to finalize the outlier removals. The case study results in Harris show that the PODM detects 28% of outages (including traffic area) compared to 17% of outages (living area only) reported by ground truth data, indicating general agreement with the proposed method.

Keywords: night light remote sensing; VIIRS DNB; outage detection; outlier removing

1. Introduction

Large-scale meteorological disasters have a serious impact on human life. After the disaster, rapid and efficient disaster assessment in the affected areas guarantees the salvation of affected people and infrastructure reconstruction. There are two conventional disaster assessment methods: on-site field investigation [1–3] and remote sensing detection [4–6]. Remote sensing detection is preferred to assess the disaster situation in the face of major disasters due to strong timeliness, wide detection range and being free of traffic isolation.

Based on the wavelength of the electromagnetic wave, traditional remote sensing detection is divided into daytime optical [7] and microwave remote sensing [8,9]. However, these two methods can only detect changes in surface morphology and building form, which means it is difficult to evaluate the impact of disasters quantitatively. The night-time light images of human living areas can directly reflect human residential activities [10,11].

Under the attack of disasters, the normal operation of infrastructure and electrical equipment in areas where people live is affected, resulting in light changes at night-time. By establishing a power outage detection model (PODM), the night light changes in cities and towns before and after the disaster can be calculated. Meteorological disaster detection is completed by assessing the power outages in the survey sites. The spatial distribution of power outage caused by meteorological disaster is detected by drawing a power outage spatial distribution map (POSDM).

Compared with traditional daytime remote sensing images, the signal of low-light remote sensing images is faint. In recent years, the improvement in photonics has witnessed significant progress in sensitivity on the space-borne optical sensor, and remote sensing at night-time has become more feasible than decades ago. Additionally, such tools are widely used in evaluating regional economic development [12–14], population distribution [15–17], power consumption [18,19], carbon dioxide emissions [20], military conflicts [21], urban scale [22–24], PM2.5 concentration [25,26], snow cover [27] and epidemic impact [28,29] detection.

At this stage, the widely used low-light remote sensing equipment includes the operational line scanner (OLS) carried by the Defense Meteorological Satellite Program (DMSP) [30] and visible infrared imaging radiometer suite (VIIRS), and the day/night band (DNB) [31] carried by the Suomi National Polar-orbiting Partnership(S-NPP) and National Oceanic and Atmospheric Administration −20(NOAA20). The VIIRS has 22 bands. Among them, the DNB band is 0.5~0.9 μm, which has a broad observing capability range from day to night. The DNB detector with 14 bits adopts three gain ranges of the high gain stage (HGS), medium gain stage (MGS) and low gain stage (LGS), realising the radiance detection range of 3×10^{-9}~0.02 W/(cm2·sr) spanning seven orders of magnitude. The VIIRS DNB is an improvement of the OLS, in which pixel resolution can be stabilised at 750 m. Thanks to the onboard calibration ability, the VIIRS DNB has high radiometric accuracy. Based on the success of the VIIRS DNB, NOAA launched the NOAA-20 satellite carrying the VIIRS DNB in November 2018 and entered the joint polar orbit of the S-NPP satellite to achieve global observation [32]. Compared with the OLS, the VIIRS DNB has improved spatial resolution (GSD), an enlarged dynamic range of radiometric detection (3×10^{-9} to 0.02 W/(cm^2·sr)), restrained scanning edge image distortion and in-orbit radiation calibration ability. Overall, the VIIRS DNB has better observation ability at night, so VIIRS DNB data were selected to build PODM and POSDM in this research.

There are many research results on disaster monitoring based on night-time images. In 1999, Shin et al. applied DMSP-OLS night light images before and after the earthquake to speculate the areas affected by the earthquake of Marmara, Turkey [33]. However, due to the poor performance of the OLS, disaster detection based on DMSP satellite images could not achieve a satisfying result.

In 2013, Cao and Shao applied the VIIRS DNB images to detect the night light radiance changes in the target area after the attack of the Derecho storm and hurricane Sandy, and better outage assessment results were acquired [34]. In 2017, Cole et al. studied hurricane Sandy [35], combining S-NPP VIIRS DNB data with geographical information such as local infrastructure distribution and surrounding population distribution. A neural network algorithm was also applied to evaluate power outages' temporal and spatial distribution quantitatively. In 2018, Fan analysed the VIIRS nearly constant contrast (NCC) environmental data record (EDR) data of the target area around the earthquake [36]. After eliminating the influence of clouds, moonlight, solar irradiance and low-quality pixels, the standard deviation change before and after the disaster was calculated to detect the affected area of disasters. In 2021, Soma took the cyclone and storm that happened in India as the research event [37]. By analysing the VIIRS DNB satellite image data, the degree of the power outage was estimated according to the night-time images. Additionally, the number of people and crops affected by the disaster was estimated by combing through the VIIRS DNB data with population and crop distribution data in the affected area. In remote sensing images, outliers generally refer to pixels whose radiance values are significantly

higher or lower than the normal range [38]. However, the impact of outliers in VIIRS DNB images on power outage detection and disaster assessment is ignored in the work above, which limits the accuracy.

Due to the tight schedule for post-disaster reconstruction, it is necessary to use the daily VIIRS DNB image data after the disaster. The occurrence of disasters is generally accompanied by severe atmospheric and ground environment change, increasing the number of outliers in the VIIRS DNB image at night. The detection accuracy will deteriorate without removing outliers in VIIRS DNB images. Compared with the previous outage detection work, the core innovation of this paper is the establishment of PODM with outlier removal, which improves outage detection accuracy. The POSDM is also drawn to detect the spatial distribution of power failure in the meteorological-disaster-affected area.

This paper studies the 2021 North American winter storm Uri and selects Harris County, Texas, as the region of interest in detecting power outages [39]. The PODM is established based on the daily night-time VIIRS DNB images from three months before and 15 days after the disaster. After filtering out the low-quality images with large satellite zenith angles or those seriously affected by cloud, the outliers in the VIIRS DNB images were also spotted and eliminated. We calculated the average radiance of pixels in the target area profile of satellite images before and after the disaster. After the lunar and atmospheric correction, the average radiance in the target area was compared with the daily radiance after the disaster. The power outage affected by the disaster was quantitatively evaluated. The result calculated by the established model was validated by the power supply data surveyed by the local power company, using it as reference truth data for this research, and the data change trend and deviation degree met the expected requirements. This verifies the feasibility of using the VIIRS DNB satellite image data to detect meteorological disasters through the established PODM. Finally, a method to draw the POSDM is proposed, which intuitively monitors the night-time light change in the affected area.

The structure of this paper is arranged as follows. Section 1 introduces the purpose, significance and overall procedure of meteorological disaster detection based on DNB night images. Section 2 introduces the selected meteorological disaster event, VIIRS DNB images, ancillary data and software used in the paper. Section 3 discusses building the PODM and drawing the POSDM based on the VIIRS DNB images. Section 4 removes and analyses the outliers in the VIIRS DNB images and finishes the power outage detection based on the PODM. The accuracy of the result is verified by comparing it with power company surveyed outage data. The spatial distribution of power outages is also analysed based on the POSDM. Section 5 summarises the overall work.

2. Materials and Methods

This section introduces the selected meteorological disaster events and the data used.

2.1. Event Selection

From 13th February to the 17th, 2021, the winter storm Uri, equivalent to a category 3 hurricane caused by an extra-tropical cyclone, attacked northern Mexico, United States, and some parts of Canada. At least 299 people were killed [40], causing USD 190 billion losses [41], and more than 5 million households and other users lost power [42].

A massive power outage occurred in Harris County, Texas, caused by Uri [39]. With a coordinate coverage of (29.50 °N~30.17 °N, −95.96 °W~ −94.91 °W), the geographical location and regional shapefile of Harris county were as shown in Figure 1. According to the census statistics surveyed in 2020, Harris County's population was 4.7 million, the most populous county in Texas and the third most populous county in the United States. Human activities at night are relatively active in this county, which is conducive to this study.
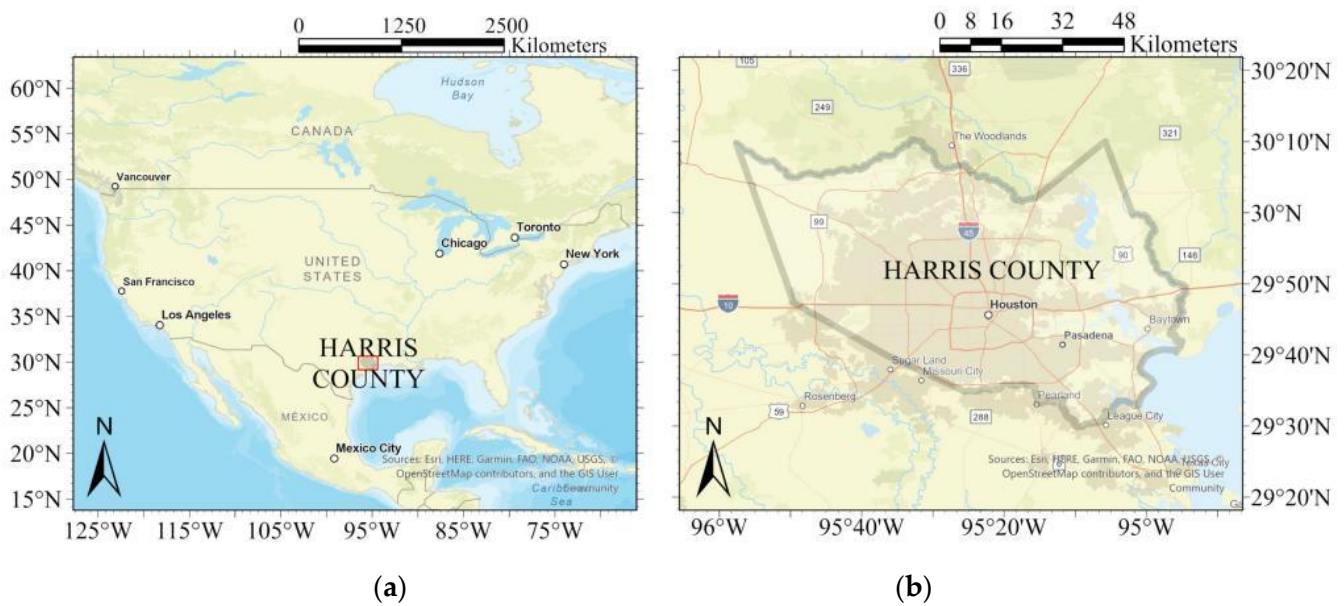
Figure 1. Geographic location map of Harris County. (**a**) Location of Harris County in the United States; (**b**) schematic diagram of Harris County administrative district boundary. ArcGIS Pro drew both figures.

2.2. VIIRS DNB Data

Carrying the VIIRS with 22 detection channels, the S-NPP and NOAA-20 satellites launched in October 2011 and November 2017, respectively, can achieve image detection with a bandwidth of 0.412~12.01 μm. Among these detection channels, the day and night band (DNB) ranges from 0.4~0.9 μm, originally designed for all-weather cloud detection from day to night. With a solar diffuser, the VIIRS DNB can be radiometric calibrated near the terminator onboard. The spatial resolution of VIIRS DNB is 750 m at the nadir. The spatial resolution is relatively stable even at the swath edge owing to the on-chip aggregation of the CCD detector. The radiance intensity range that the VIIRS DNB can observe is from 3×10^{-9} to 0.02 W/(cm^2·sr), which spans 7 magnitudes. To meet the required illumination intensity range from the strongest direct sunlight in the day to the reflected moonlight from a quarter moon at night, the VIIRS DNB adopts three gain stages ranging from the high gain stage (HGS) to the medium gain stage (MGS) and the low gain stage (LGS). The bit width of the HGS is 14, and it is 13 for the MGS and LGS. According to the radiance change in the observed target area, the gain stage is automatically selected by the onboard algorithm. While avoiding image saturation caused by strong sunlight during the daytime, images with low illumination under the moonlight at night can be observed. Overall, the VIIRS has the advantages of onboard calibration, large observation dynamic range, restricted swath edge image distortion and high spatial coverage [43]. We selected DNB images three months before the disaster and 15 days after the disaster for power outage detection. Selecting the data of the first three months of the disaster could ensure enough data and avoid errors caused by large changes in the accumulated ground lighting infrastructure due to the long time span. DNB images in the 15 days after the disaster could fully reflect the trend of power outage recovery. After the above screening and processing processes, there were a total of 54 VIIRS DNB images finally used for power outage detection, including 29 NOAA-20 and 25 S-NPP images. The actual time range of DNB images used is from 12 November 2020 to 8 March 2021.

The data source URL link is https://www.avl.class.noaa.gov/saa/products/welcome/ (available on 1 October 2022).

2.3. AOD Data

In order to eliminate the influence of atmospheric conditions on power outage detection, aerosol optical depth (AOD) was studied. AOD data were acquired through the sun photometer applied by the AERONET ground station. According to the different processing levels, AOD data were divided into three levels: level 1.0, level 1.5 and level 2.0, which corresponded to the original data of the sun photometer, the data after cloud removal and preliminary correction and the data after complete correction, respectively. AOD data from the AERONET station of the University of Houston in Harris County were selected, whose longitude and latitude coordinates are (29.718°N and 95.342°W). Since level 1.0 data were seriously affected by clouds and level 2.0 data were unavailable, level 1.5 AOD data from 15 November 2020 to 2 March 2021 were used [44,45].

The data source URL link is https://aeronet.gsfc.nasa.gov/ (available on 1 October 2022).

2.4. Cloud Mask Data

This work used the SNPP VIIRS incarnation of the Cloud Properties continuity product (CLDPROP) to eliminate the influence of clouds on meteorological disaster detection. CLDPROP was installed in the VIIRS, which could provide the possibility of each pixel being disturbed by clouds in the target area. The probability was divided into four levels: confident cloudy "0", probably cloudy "1", probably clear "2" and confident clear "3". To synchronise with VIIRS DNB night-time images, this work applied CLDPROP products provided by the VIIRS on S-NPP and NOAA-20. Data and time of CLDPROP were also synchronised with the DNB satellite images [46].

The data source URL link is https://ladsweb.modaps.eosdis.nasa.gov/search/ (available on 1 October 2022).

2.5. Surface Reflectance Data

The surface reflectance of the target area was required to calculate the stray moonlight reflected into the VIIRS sensor. MOD09A1 surface reflectance product observed by MODIS was selected. This product is level 2 data. After atmospheric correction, it could provide 8-day average surface reflectance with 1 km spatial resolution. Surface reflectance data corresponding to the coordinate of Harris County and the study date were used. MOD09A1 contains a total of 7 band channels, and the surface reflectance data of 1 (620~670 nm), 2 (841~876 nm) and 4 (545~565 nm) channels that overlapped with the band range of DNB (500~900 nm) were selected [47].

The data source URL link is https://ladsweb.modaps.eosdis.nasa.gov/search/ (available on 1 October 2022).

2.6. Outages Data

Power outage data provided by Center Point Energy (CPE) were selected to verify the result from established data. As the major power supplier in Harris county, CPE tracked 1.95 million users in Harris County and could provide an hourly outage percentage during the disaster. Since the number of users occupies the main part of Harris County, it could embody the power outages caused by disasters. There were only sporadic small-scale power outages in Harris County before the disaster, which had little impact on the whole. Power outage data from 9 February 2021 to 10 March 2021, near the disaster, were mainly studied. The data source URL link is https://poweroutage.us/ (available on 1 January 2023), and the historical data can be obtained by contacting customer service.

2.7. MODTRAN

The atmospheric transmittance was calculated using MODTRAN 5.3 software [48]. As the professional software used to analyse the atmospheric radiation transmission characteristic, MODTRAN can calculate the atmospheric radiation transmittance in the range of 0.2~100 μm wavebands. This study calculated atmospheric transmittance in the DNB (0.5~0.9 μm) band according to the given AOD atmospheric parameters.

2.8. MT2009

Miller and Turner established the MT2009 model to calculate the lunar irradiance at the top of atmosphere (TOA), which can be further utilised to eliminate stray lunar light in DNB images [34]. MT2009 calculates the irradiance spectral distribution with 1 nm spectral resolution in the range of 0.3–1.2 μm based on lunar surface albedo, the sun–moon–earth geometric relationship and lunar phase angle for the given date and time. Lunar stray light radiance at TOA can be acquired by MT2009 irradiance spectral and DNB satellite spectral response function convolution [49].

3. Methodology

The PODM was established, as shown in Figure 2. After the event, ROI and date range selection, the following steps occurred which are described below.
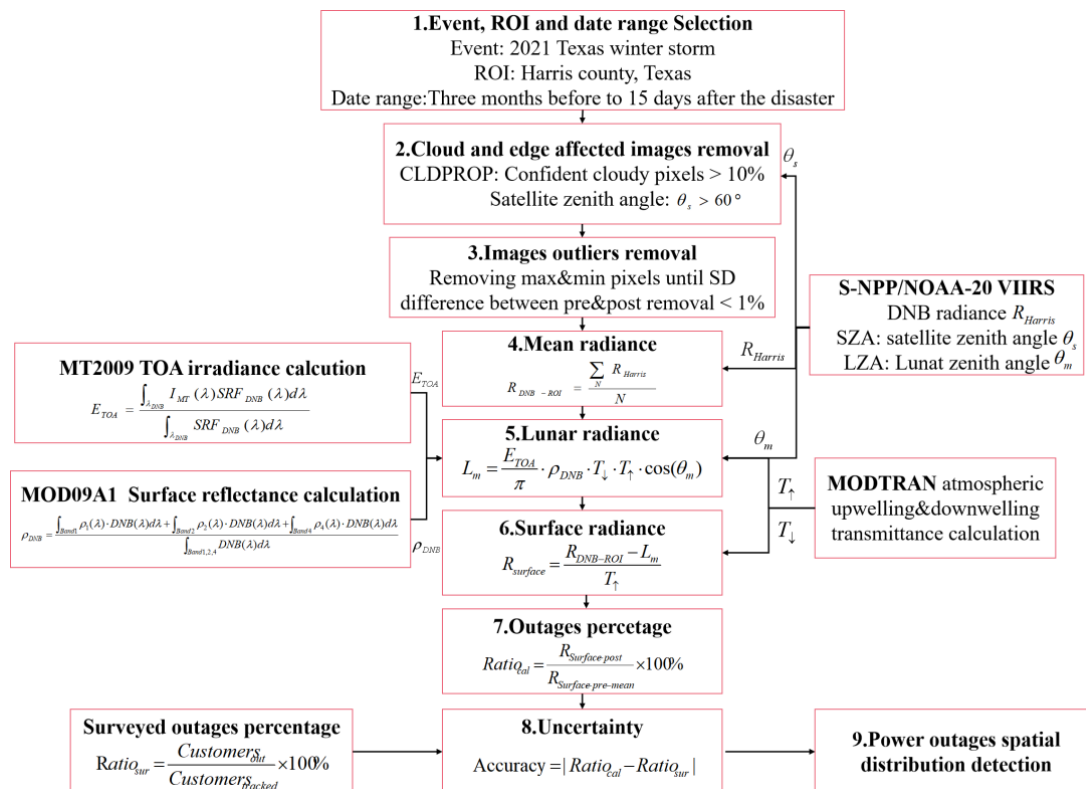

Figure 2. PODM flow chart.

3.1. Low-Quality DNB Satellite Image Screening

It was necessary to screen out some low-quality satellite images to ensure the quality of the final results. The data quality of the target area at the scanning image edge was restricted. We screened out DNB images with a satellite zenith angle greater than 60° to eliminate the influence of deformed pixels at the scanning edge [50]. CLDPROP synchronised with DNB images was used to restrain the influence of clouds. DNB satellite images with more than 10% of absolute cloud pixels in the Harris County shapefile were removed. Figure 3 shows the distribution diagram of the cloud mask in the DNB satellite image data.
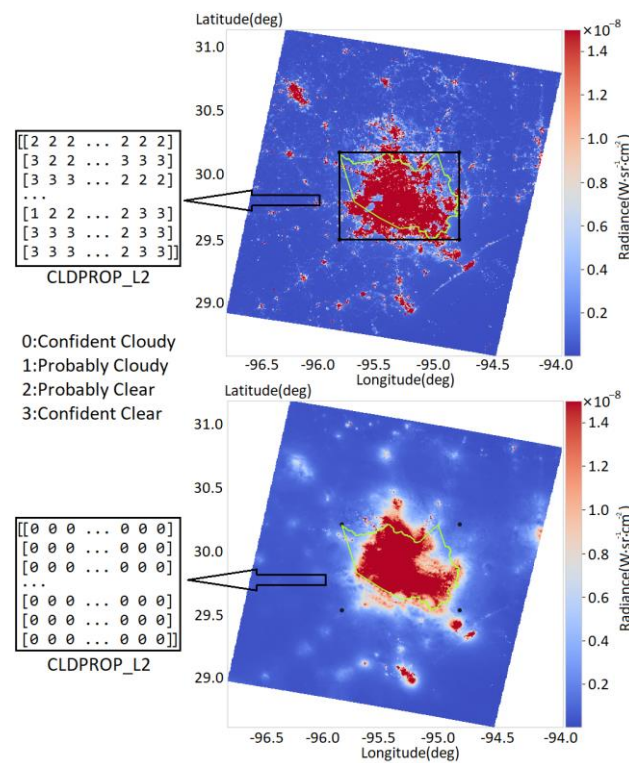
Figure 3. Schematic diagram of the corresponding relationship between CLDPROP and VIIRS DNB images.

3.2. Outlier Removing

Severe meteorological and environmental variations in the target area before and after the disaster will induce many outliers in the DNB satellite image, affecting the accuracy of power outage detection. An iterative method was used to achieve the removal of outliers. The maximum and minimum radiance values in Harris county were removed simultaneously until the standard deviation difference in pixel radiance points before and after removal was less than 1%. This method was proposed by Baugh and first applied to the outlier removal of DMSP-OLS images [51]. Then, it was also applied to the VIIRS DNB satellite image by Elvidge [38] and Yuan [52] to realise outlier removal.

3.3. Average Radiance Calculation

After removing outliers, we calculated the average radiance of DNB images in Harris County as shown in Formula (1).

$$R_{DNB-ROI} = \frac{\sum\limits_{N} R_{DNB}}{N} \tag{1}$$

where R_{DNB} is the radiance value of each pixel inside the shapefile of the target area, and N is the total amount of all of the pixels in the shapefile.

3.4. Atmospheric Correction

During the transmission of reflected lunar light and night-time city light in the atmosphere, it will be scattered and absorbed by gas molecules, aerosols and water particles. Therefore, it was necessary to carry out an atmospheric correction to obtain target radiance more accurately. Many parameters affect atmospheric transmittance, including CO_2 and water vapour concentration, among which the key variable is AOD [53]. AOD data in 1020 nm, 870 nm, 675 nm and 440 nm bands during the study disaster period were used [44]. The AOD data of four bands at the imaging time of the DNB images at night were obtained using linear interpolation between data at the nearest morning and dusk

time [54]. The AOD data of 550 nm required by MODTRAN were acquired by least square regression of AOD data in 4 bands [55]. With the lunar and satellite zenith angles provided by the VIIRS DNB images, MODTRAN was applied to obtain the upwelling and downwelling atmospheric transmittance.

3.5. Lunar Correction

The stray lunar light had a serious impact on the DNB satellite image. The lunar correction was realised by establishing a nocturnal atmospheric radiation model, as shown in Figure 4. Lunar stray light is mainly sunlight reflected from the lunar surface to the VIIRS DNB sensor. In order to calculate the stray lunar light, it was necessary to consider the effects of the earth's surface reflectance, atmospheric transmittance, lunar phase angle, the spectral response curve of the VIIRS DNB sensor and the geometric path of the sun/moon/earth. The MT2009 model proposed by Miller and Turner et al., as shown in Formula (2), was used to calculate the lunar irradiance TOA [49].

$$E_{TOA} = \frac{\int_{\lambda_{DNB}} I_{MT}(\lambda) SRF_{DNB}(\lambda) d\lambda}{\int_{\lambda_{DNB}} SRF_{DNB}(\lambda) d\lambda} \quad (2)$$

where E_{TOA} is the lunar irradiance at TOA obtained by convolution of the DNB sensor spectral response function and lunar radiation spectral response function, $I_{MT}(\lambda)$ is the spectral distribution function of lunar irradiance calculated by the MT2009 model, λ_{DNB} is the VIIRS DNB sensor spectral range, which is 0.5~0.9 μm, and $SRF_{DNB}(\lambda)$ is the spectral response function of the VIIRS DNB sensor. Based on the lunar radiance model proposed by Cao [34], Formula (3) is established to calculate the stray lunar radiance using the VIIRS DNB sensor L_m. The influence of atmospheric transmittance is added to the model.

$$L_m = \frac{E_{TOA}}{\pi} \cdot \rho_{DNB} \cdot T_{\downarrow} \cdot T_{\uparrow} \cdot \cos(\theta_m) \quad (3)$$

where θ_m is the zenith angle of the moon, which can be obtained from the VIIRS DNB image. $T_{\uparrow}$ and $T_{\downarrow}$ are upwelling and downwelling atmospheric transmittance, respectively.
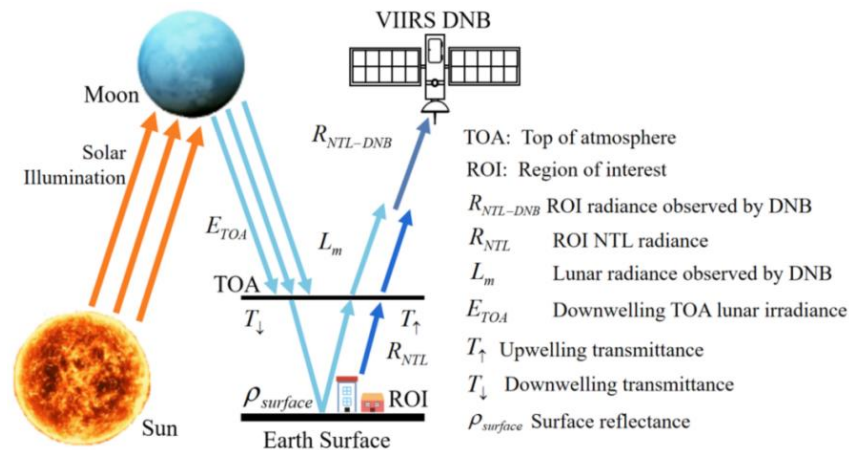

Figure 4. Schematic diagram of nocturnal atmospheric radiation model.

$\rho_{surface}$ is the surface reflectance weighted with DNB spectral response function, calculated as (4).

$$\rho_{DNB} = \frac{\int_{Band1} \rho_1 \cdot SRF_{DNB}(\lambda) \cdot d\lambda + \int_{Band2} \rho_2 \cdot SRF_{DNB}(\lambda) \cdot d\lambda + \int_{Band4} \rho_4 \cdot SRF_{DNB}(\lambda) \cdot d\lambda}{\int_{Band1,2,4} SRF_{DNB}(\lambda) \cdot d\lambda} \quad (4)$$

where ρ_2 and ρ_4 were the average values of surface reflectance of channel 1 (620~670 nm), 2 (841~876 nm) and 4 (545~565 nm) in MOD09A1. The correspondence between the se-

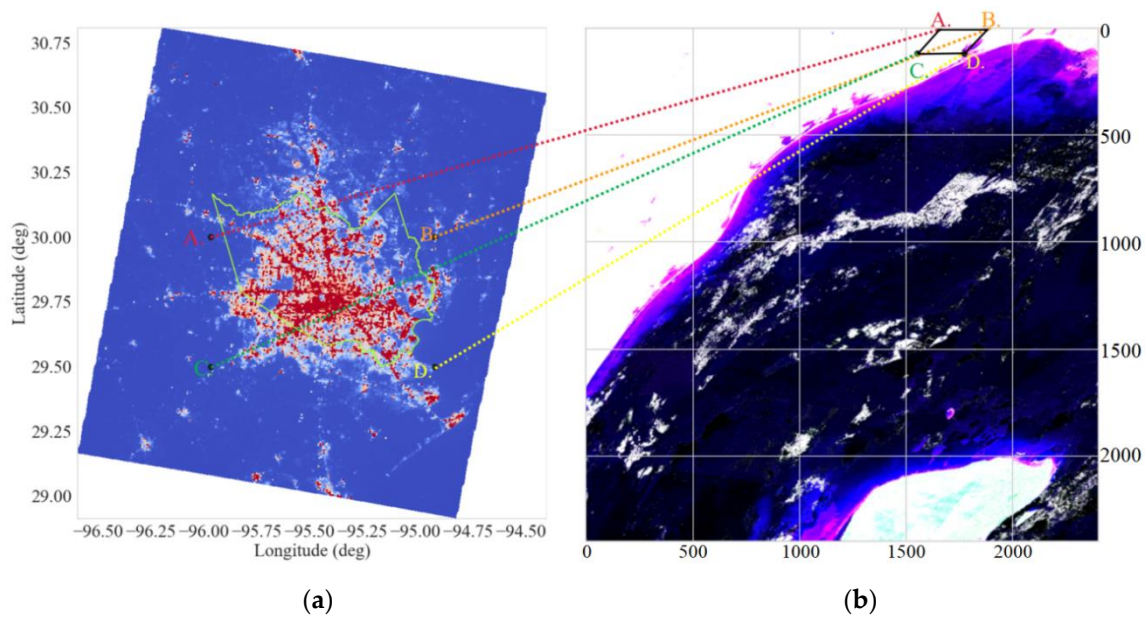lected MOD09A1 surface reflectance area and the VIIRS DNB image is shown and illustrated in Figure 5.

Figure 5. MOD09A1 surface reflectance average area coordinate correspondence. (**a**) Night time image of VIIRS DNB in Harris County; (**b**) MOD09A1 surface reflectance of 8-day 1-, 2- and 4-channel stacked RGB images. The corresponding relationship is as follows: A. (−95.97,29.80) to (1653,0); B. (−94.91,30.00) to (1873,0); C. (−95.97,29.50) to (1553,120); D. (−94.91,29.50) to (1774,120).

The average radiance of Harris County with lunar correction was calculated as Formula (5). The influence of BRDF and path radiation was ignored. Since the satellite zenith angle of the DNB images used was less than 60, the variance in artificial light source caused by anisotropy was relatively stable [56,57]. So, the anisotropic characteristic of artificial light in the ROI area was ignored.

$$R_{NTL} = \frac{R_{DNB-ROI} - L_m}{T_\uparrow} \tag{5}$$

3.6. Power Outage Detection

The power outage rate $Ratio_{outages}$ in the affected area was calculated as Formula (6).

$$Ratio_{outages} = \frac{R_{NTL-post}}{R_{NTL-pre-mean}} \times 100\% \tag{6}$$

where $R_{NTL-post}$ is the daily average radiance in the Harris County shapefile with atmospheric and lunar correction being post-disaster. $R_{NTL-pre-mean}$ is the average value of R_{NTL} in the three months before the disaster.

3.7. Bias Calculation

Finally, the bias of the detected power outage rate was estimated as shown in Formula (7).

$$Bias = |Outages_{cal} - Outages_{Sur}| \times 100\% \tag{7}$$

where $Outages_{Sur}$ is the surveyed power outage percentage. $Outages_{Cal}$ is the calculated power outage rate based on VIIRS DNB images.

3.8. Power Outage Spatial Distribution Detection

A POSDM can guide post-disaster reconstruction work intuitively. A method to detect the spatial distribution of power outages based on VIIRS DNB images was introduced. However, the difficulty was that the longitude and latitude positions of the pixel points in each VIIRS DNB image did not correspond, so the arithmetic operation could not be performed directly. This paper solves this problem according to the steps shown in Figure 6. It is generally divided into five steps: (1) Select the region of interest (ROI), and determine the latitude and longitude range for spatial detection. (2) Stack the VIIRS DNB satellite images before the disaster. (3) Extract the longitude and latitude of each pixel in the ROI of the post-disaster VIIRS DNB images in sequence. Calculate the average radiance of the stacked image within the set distance of the corresponding extracted post-disaster points so that random noise, such as atmospheric variation, stray lunar light, biomass burning and lightning, can be restrained. Take the average result as the value of each pixel, and acquire the averaged VIIRS DNB image before the disaster. (4) Calculate the radiance difference in the corresponding pixel points before and after the disaster. Additionally, take the value greater than zero to obtain the difference map. Set the pixel value smaller than zero in the difference calculation as zero to reduce the interference to power failure detection. (5) Adjust the dynamic display range of the difference map, and obtain the POSDM.
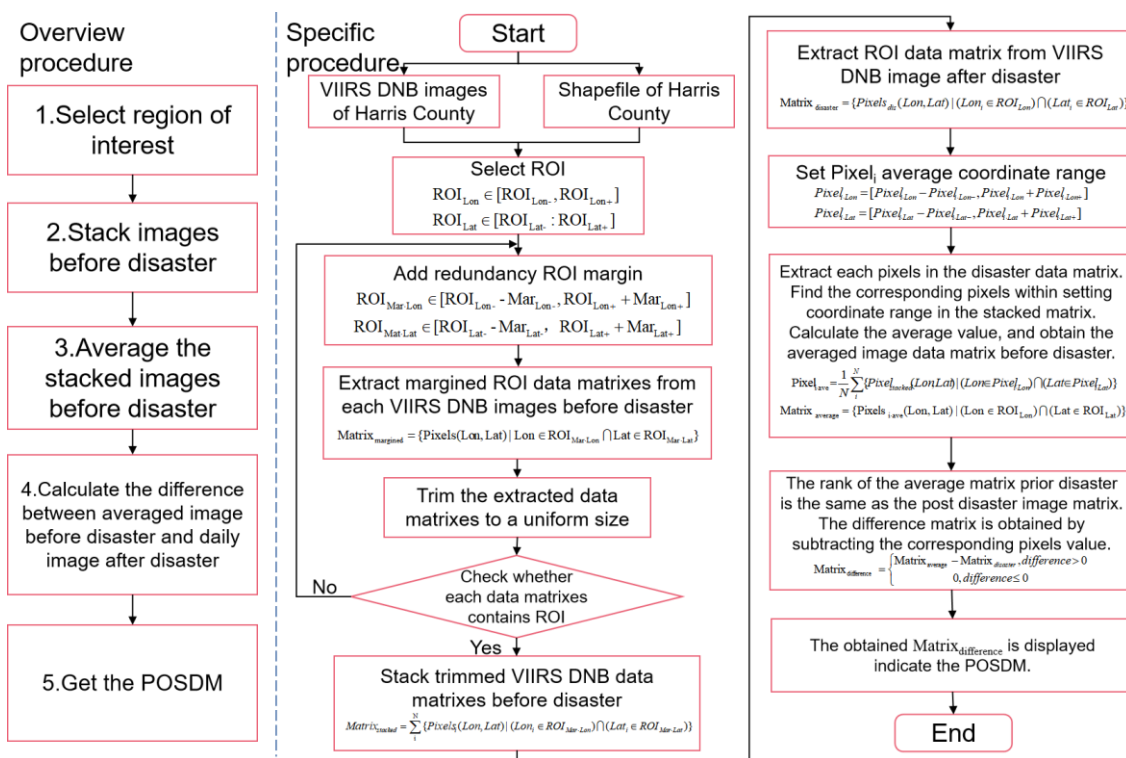

Figure 6. POSDM flow chart.

According to Figure 6, the process of drawing the Harris County POSDM is shown in Figure 7. First, set the ROI centre as ($-95.5°$W, $29.86°$N) and the longitude and latitude ranges as $0.75°$. Then, stack 41 VIIRS DNB satellite images containing ROI before the disaster. In order to ensure the integrity of ROI data, the longitude and latitude range of the image margin must be appropriately increased before stacking. According to the longitude and latitude position of each pixel in the post-disaster image, calculate the average value of all pixels within $0.001°$ in longitude and latitude in the stacked image at the corresponding coordinates to obtain the averaged image before the disaster. Acquire the difference map by subtracting the values of the pixel points at the corresponding positions of the averaged image before the disaster and the daily image after the disaster. Finally,

set the display range of the difference map to $1 \times 10^{-7}(\text{W} \times \text{sr}^{-1} \times \text{cm}^{-2})$, and acquire the POSDM. The greater the difference in the map, the more severe the power failure caused by meteorological disasters.
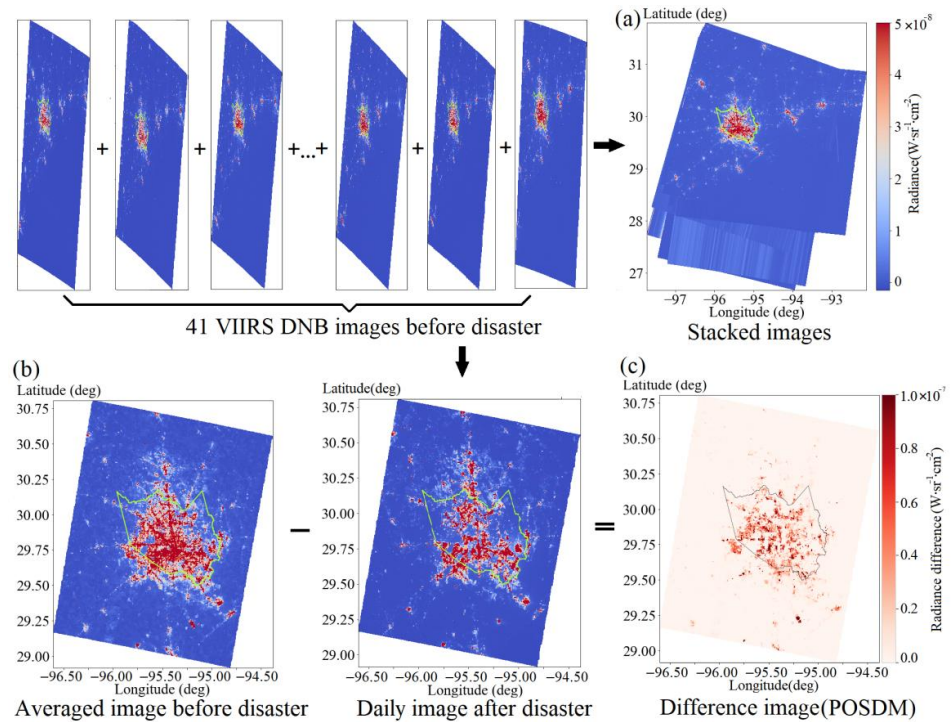

Figure 7. The process of drawing the POSDM. Ways to make (**a**) stacked image, (**b**) averaged image and (**c**) difference image.

4. Results and Discussion

4.1. Outlier Discussion

The number of outliers removed in each VIIRS DNB image according to the above method is shown in Figure 8. The blue dotted line corresponds to the date of the meteorological disaster. The number of outliers increased sharply after the occurrence of meteorology and then showed a downward trend.
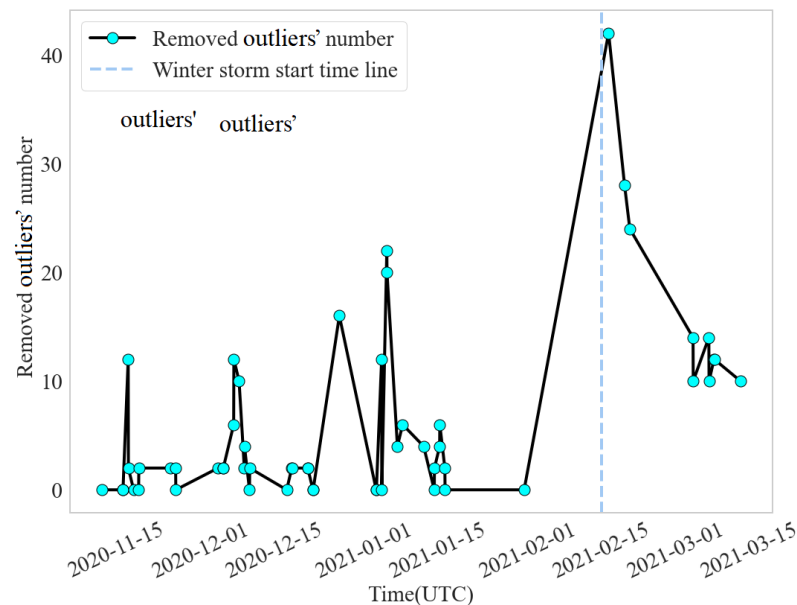

Figure 8. Removed outliers' numbers in each VIIRS DNB curve plot.

A total of six groups of DNB images before and after the disaster were selected for the research to study the impact of meteorological disasters on outliers. The numbers and values of outliers are shown in Table 1.

Table 1. Summary table of outliers removed in six VIIRS DNB images before and after the disaster.

Date (UTC)	Time (UTC)	Outliers' Number	Min. Outlier Range (W·cm^{-2}·sr^{-1})	Max. Outlier Range (W·cm^{-2}·sr^{-1})
16 January 2021	07:34:18	2	6.48×10^{-10}	5.52×10^{-7}
16 January 2021	08:25:30	0	/	/
31 January 2021	07:56:18	0	/	/
16 February 2021	07:55:06	42	5.45×10^{-10}~6.45×10^{-10}	6.27×10^{-7}~2.94×10^{-5}
19 February 2021	08:39:19	28	4.35×10^{-10}~6.29×10^{-10}	5.96×10^{-7}~4.28×10^{-6}
20 February 2021	08:21:50	24	3.24×10^{-10}~4.20×10^{-10}	5.39×10^{-7}~2.32×10^{-6}

Due to the drastic environmental variation in the atmosphere and surface caused by the disaster, the number of outliers increased sharply. With the recovery of the affected environment, the number of outliers gradually decreased after the disaster. In the DNB image on 16 February 2021, the first day after the disaster, there were 42 outliers detected in total. The minimum outliers are within 10^{-10} orders of magnitude, and the maximum outliers are within the range of 10^{-7}~10^{-5}. The magnitude of the maximum outliers differs from the average value of 10^{-8}, so outliers will seriously affect the accuracy of power outage detection. Removing outliers from DNB images is of great significance to the accuracy of meteorological disaster detection.

The maximum and minimum outliers' positions in the DNB images are shown in Figure 9. The cyan plus sign in the figure represents the minimum outliers, and the yellow plus sign represents the maximum outliers. Except for the 31 January 2021 satellite image, the minimum outliers of each image are mainly located in the northwest corner of Harris County. It may be that the human activities in this area are sparse, the light intensity at night is low and the signal to noise ratio of the data measured by the DNB sensor in this area is low, leading to the generation of minimum outliers. The maximum outliers are mainly distributed in the eastern part of Harris County. After the disaster, the number of maximum outliers in the image increased, partly due to the frequent human activities at night and the high-intensity urban lights at night. After meteorological disasters, the atmospheric and surface environment changed dramatically, increasing the number of maximum outliers in this area. Although the number of outliers is negligible compared to the total number of pixels in the target area, their value differs greatly from the normal value range, which has a certain impact on the calculation result of the average radiance. Therefore, each image's maximum and minimum outliers should be removed to obtain an accurate result.

4.2. Harris County Outages Degree

According to the power outage detection map set up in the previous section, power outage detection was carried out in the target area. The schematic diagram of radiance results is shown in Figure 10a. The solid black line in Figure 10a shows the average value of night image radiance within the target profile. The solid purple line indicates the stray lunar radiance. The solid blue line is the average radiance curve after lunar correction. The green line corresponds to the average radiance after lunar and atmospheric correction, that is, the final result of the PODM radiance. The solid red line in Figure 10a shows the average value of night image radiance within the target profile. The change trends of black, green and blue curves are the same. They all show a significant attenuation trend after meteorological disasters, which can effectively reflect the power outage in the disaster area. A 550 nm AOD data curve obtained from 4-band AOD data of the ground station is shown in Figure 10b. The changing trend of 550 nm AOD data is consistent with the change in radiance before and after atmospheric correction in the study area. The lunar phase angle

and lunar zenith angle obtained from the DNB dataset are shown in Figure 10c. The solid yellow line is the lunar phase angle, and the solid light blue line indicates the lunar zenith angle. The changing trend of the lunar phase angle is the same as that of the lunar zenith angle. With the decrease in the two values, the amount of lunar stray light becomes larger, which is consistent with the actual change regularity.
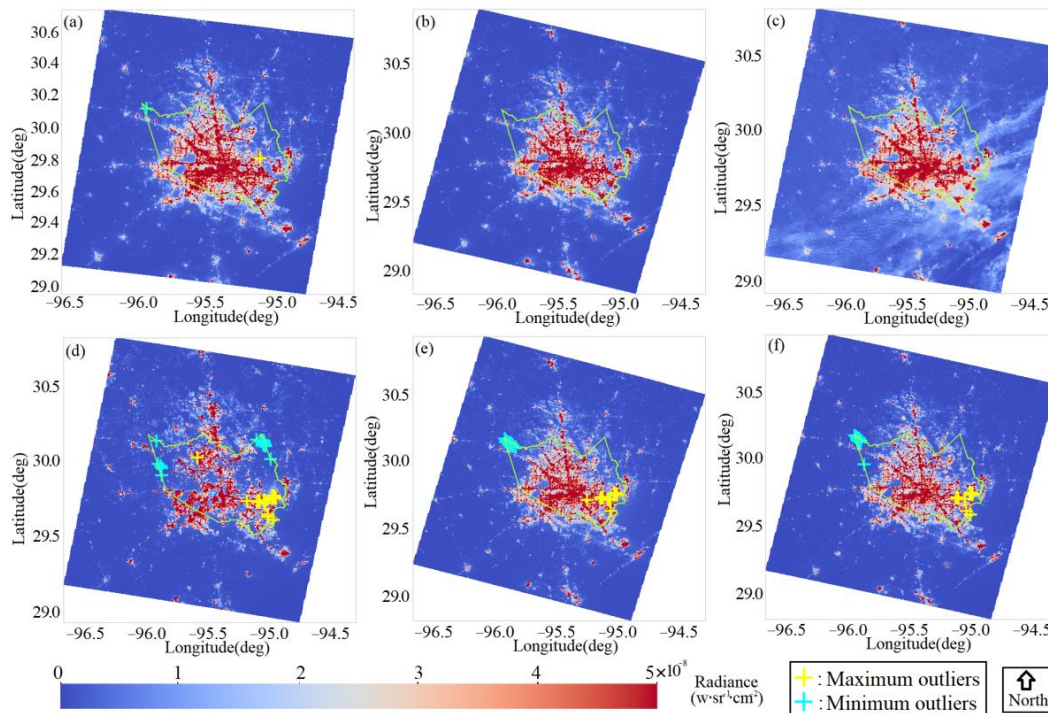

Figure 9. Outliers' positions in 6 VIIRS DNB images before and after the disaster. The corresponding observation dates are as follows: (**a**) 15 January 2021; (**b**) 16 January 2021; (**c**) 31 January 2021; (**d**) 16 February 2021; (**e**) 19 February 2021; (**f**) 20 February 2021.

The average radiance values of the six individual VIIRS DNB images in the target area closest to the disaster are summarised in Table 2. The table includes three pre-disaster and three post-disaster data. The first row of the table shows the relative time difference between the observation time of each image and the occurrence time of meteorological disasters in days. Corrected rad., Outages Cal. and Outages Sur. in the first column of the table represent the atmospheric corrected ROI mean radiance, the PODM calculated outage percentage and the surveyed outage percentage, respectively. The percentage of power outages calculated by PODM one day after the disaster was 28.48%. Additionally, the percentage of residents' power outages one day after the disaster was 17.34%, according to the data provided by the power company. The deviation was 11.14% according to Formula (1).

Table 2. Summary table of six VIIRS DNB image results from the PODM before and after the disaster.

| Relative Time Point of Disaster	Prior 30 Days	Prior 30 Days	Prior 15 Days	Post 1 Day	Post 4 Days	Post 5 Days
Date (UTC)	16 January 2021	16 January 2021	31 January 2021	16 February 2021	19 February 2021	20 February 2021
Time (UTC)	07:34:18	08:25:30	07:56:18	07:55:06	08:39:19	08:21:50
Corrected rad. ($10^{-8} \cdot$W$\cdot$sr$^{-1} \cdot$cm^{-2})	4.20692	4.45718	3.75163	3.16993	4.15621	3.71420
Outages Cal. (%)	\	\	\	28.48%	\	\
Outages Sur. (%)	\	\	\	17.34%	0.10%	0.01%
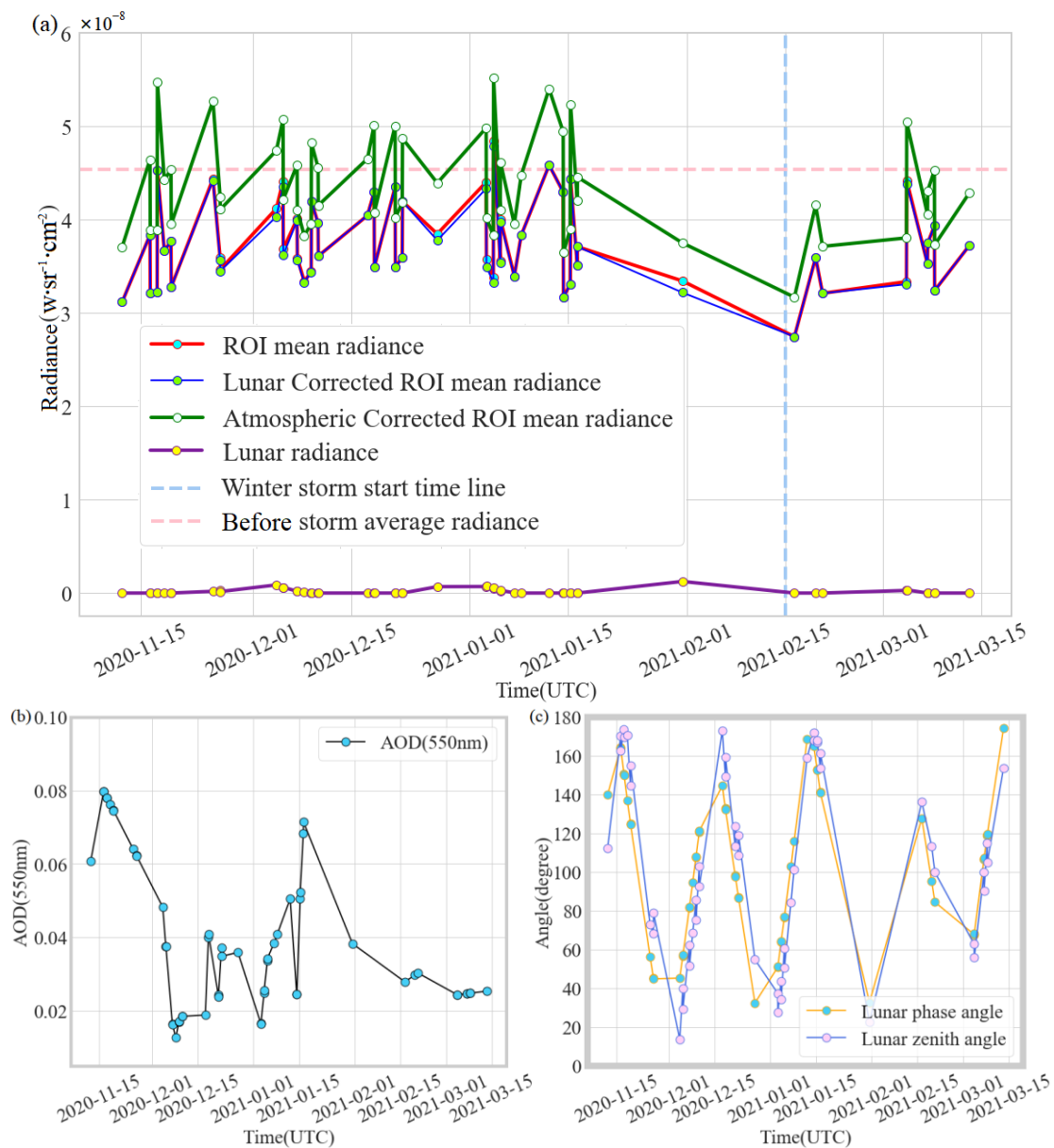
Figure 10. (**a**) The PODM results from the plot, (**b**) AOD (550 nm) data derived from the AERONET station AOD data of the University of Houston and (**c**) lunar phase angle and lunar zenith angle obtained from VIIRS DNB dataset. All of the above plots range from three months before the disaster to 15 days after.

4.3. Outage Spatial Distribution Analyses

In Figure 11, in addition to the serious power outage in the urban residential areas, the roads connecting the city centre also suffered serious power outages. There were four roads seriously affected, including Katy Fwy, Northwest Fwy, Tomball Pkwy and North Fwy. There were two main reasons for road power failure. (1) The street lamps were extinguished due to line damage. (2) Road traffic was detained by bad weather, so the number of vehicles running at night was reduced and, as a result, the illumination from vehicles was reduced. However, the power outage on the road was not counted by the power supply company, which also explains why the power outage detected by the PODM was higher than the referenced surveyed power outage by the local company. However, with the current spatial resolution (750 m), it was impossible to exclude the power outage of roads using the current methods.
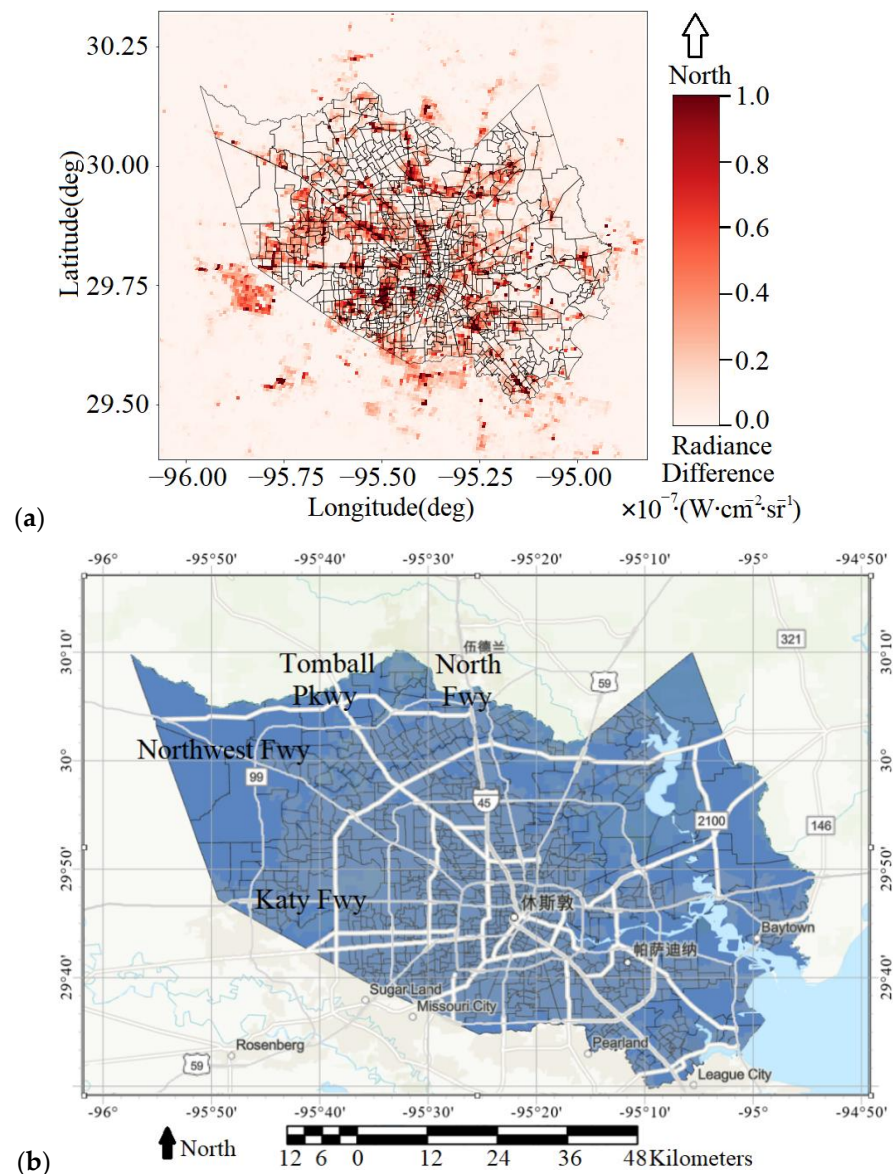
(a)

(b)

Figure 11. (**a**) Power outage spatial distribution map. Radiance difference between average VIIRS DNB images before the disaster (12th November 2020–31 January 2021, contains 19 NOAA-20 and 22 S-NPP VIIRS DNB images) and daily VIIRS DNB image post-disaster (16th February 2022, 1-day post-disaster). (**b**) ArcGIS Pro draws a distribution map of main roads and urban areas in Harris County. Where "休斯顿", "伍德兰", and "帕萨迪纳" stands for "Houston", "Woodlands", and "Pasadena".

5. Conclusions

This paper takes the winter storm Uri in Harris County, Texas, on February 15th, 2021, as the research object. Affected by the disaster, the urban power facilities were damaged. By analysing the low-illuminance remote sensing images at night, power outage detection in the disaster area could be realised. A meteorological disaster spatiotemporal detection method based on VIIRS DNB night-time images was proposed. The power outage degree and spatial detection were realised by building the power outage detection model (PODM) and drawing the power outage spatial distribution map (POSDM). The PODM was established as follows. First, the low-quality images with the target area having a large satellite zenith angle (SZA) or being affected by clouds were filtered. Second, outliers in the DNB images were detected and removed. Then, atmospheric and lunar correction were achieved based on the atmospheric radiation transfer model at night. Finally, the difference in radiance before and post-disaster were analysed. By iteratively eliminat-

ing the maximum and minimum values in the image until the standard deviation change was less than 1%, a total of 42 outliers were eliminated after the disaster, and the power outage detection accuracy was improved. The PODM calculated power outage one day after the disaster was 28.48%, and the power outage truth rate was 17.34%, surveyed by the power company, so the deviation was 11.14%. This can effectively reflect the extent of the power outages and realise the degree of detection of meteorological disasters. Spatial detection of meteorological disasters was realised by drawing the POSDM. The POSDM shows the difference between the VIIRS DNB images before and after the disaster through two-dimensional images. The greater the difference in the POSDM, the more obvious the change in urban light intensity at night, and the resulting power outages are serious. According to the POSDM detection, in addition to serious power outages in residential areas, power outages on roads were also serious. However, road power outages generally referred to the power outages of street lamps and a reduction in traffic flow. The power company did not count road outages in their on-site investigation, so this also explains why the detection value of PODM is higher than the result surveyed by the power company.

Author Contributions: Conceptualisation, H.C., S.Q. and Y.C.; methodology, H.C., S.Q. and Y.C.; validation, H.C., S.Q., Y.W. and Y.C.; writing—original draft preparation, H.C., S.Q. and Y.C.; writing—review and editing, H.C., S.Q., Y.W., Y.Z., Z.L., K.K., J.J. and Y.C. All authors have read and agreed to the published version of the manuscript.

Data Availability Statement: The data used in this study can be accessed through the links provided in Section 2.

Conflicts of Interest: The authors declare no conflict of interest.

References

1. Tanaka, H.; Nakagawa, H.; Ishino, K.; Yano, S.; Nawarathna, B.; Yasuda, H.; Watanabe, Y.; Hasegawa, K. Field investigation of disasters in sri lankan rivers caused by sumatra earthquake tsunami. *Proc. Hydraul. Eng.* **2006**, *50*, 577–582. [CrossRef]
2. Ding, M.-T.; Cheng, Z.-L.; Wang, Q. Coupling mechanism of rural settlements and mountain disasters in the upper reaches of Min River. *J. Mt. Sci.* **2014**, *11*, 66–72. [CrossRef]
3. Zhou, H.; Che, A.; Wang, L.; Wang, L. Investigation and mechanism analysis of disasters under Hokkaido Eastern Iburi earthquake. *Geomat. Nat. Hazards Risk* **2021**, *12*, 1–28. [CrossRef]
4. Tsai, F.; Hwang, J.-H.; Chen, L.-C.; Lin, T.-H. Post-disaster assessment of landslides in southern Taiwan after 2009 Typhoon Morakot using remote sensing and spatial analysis. *Nat. Hazards Earth Syst. Sci.* **2010**, *10*, 2179–2190. [CrossRef]
5. Wang, J.; Qin, Q.; Zhao, J.; Ye, X.; Feng, X.; Qin, X.; Yang, X. Knowledge-Based Detection and Assessment of Damaged Roads Using Post-Disaster High-Resolution Remote Sensing Image. *Remote Sens.* **2015**, *7*, 4948–4967. [CrossRef]
6. Li, S.; Sun, D.; Goldberg, M.D.; Sjoberg, B.; Santek, D.; Hoffman, J.; DeWeese, M.; Restrepo, P.; Lindsey, S.; Holloway, E. Automatic near real-time flood detection using Suomi-NPP/VIIRS data. *Remote Sens. Environ.* **2018**, *204*, 672–689. [CrossRef]
7. Lu, L.; Guo, H.; Corbane, C.; Pesaresi, M.; Ehrlich, D. Rapid Damage Assessment of Buildings with VHR Optical Airborne Images in Yushu Earthquake. In Proceedings of the International Conference on Remote Sensing IEEE, Nanjing, China, 1–3 June 2012. [CrossRef]
8. Brunner, D.; Bruzzone, L.; Lemoine, G. Change detection for earthquake damage assessment in built-up areas using high-resolution optical and SAR imagery. In Proceedings of the IEEE International Geoscience & Remote Sensing Symposium IEEE, Honolulu, HI, USA, 25–30 July 2010; pp. 3210–3213.
9. Rosen, P.A.; Hensley, S.; Joughin, I.R.; Li, F.K.; Madsen, S.N.; Rodriguez, E.; Goldstein, R.M. Synthetic aperture radar interferometry. *Proc. IEEE* **2000**, *88*, 333–382. [CrossRef]
10. Ferrentino, E.; Marino, A.; Nunziata, F.; Migliaccio, M. A dual–polarimetric approach to earthquake damage assessment. *Int. J. Remote Sens.* **2018**, *40*, 197–217. [CrossRef]

11. Elvidge, C.D.; Baugh, K.E.; Kihn, E.A.; Kroehl, H.W.; Davis, E.R. Mapping city lights with nighttime data from the DMSP Operational Linescan System. *Eng. Remote Sens.* **1997**, *63*, 727–734.
12. Zhang, J. Research on Regional Urban Economic Development by Nightlight-time Remote Sensing. *arXiv* arXiv:2105.10459, 2020.
13. Li, Q.; Shi, X.; Wu, Q. Effects of China's ecological restoration on economic development based on Night-Time Light and NDVI data. *Environ. Sci. Pollut. Res.* **2021**, *28*, 65716–65730. [CrossRef] [PubMed]
14. Yuan, D.; Jiang, H.; Guo, W.; Cui, X.; Wu, L.; Wu, Z.; Wang, H. Regression Analysis and Comparison of Economic Parameters with Different Light Index Models under Various Constraints. *Sensors* **2021**, *21*, 7561. [CrossRef] [PubMed]
15. Zhao, N.; Samson, E.L.; Liu, Y. Population bias in nighttime lights imagery. *Remote Sens. Lett.* **2019**, *10*, 913–921. [CrossRef]
16. Hall, O.; Bustos, M.F.A.; Olén, N.B.; Niedomysl, T. Population centroids of the world administrative units from nighttime lights 1992-2013. *Sci. Data* **2019**, *6*, 235. [CrossRef] [PubMed]
17. You, H.; Jin, C.; Sun, W. Spatiotemporal Evolution of Population in Northeast China during 2012–2017: A Nighttime Light Approach. *Complexity* **2020**, *2020*, 3646145. [CrossRef]
18. Sahoo, S.; Gupta, P.K.; Srivastav, S.K. Comparative analysis between VIIRS-DNB and DMSP-OLS night-time light data to estimate electric power consumption in Uttar Pradesh, India. *Int. J. Remote Sens.* **2019**, *41*, 2565–2580. [CrossRef]
19. Shi, K.; Chen, Y.; Yu, B.; Xu, T.; Yang, C.; Li, L.; Huang, C.; Chen, Z.; Liu, R.; Wu, J. Detecting spatiotemporal dynamics of global electric power consumption using DMSP-OLS nighttime stable light data. *Appl. Energy* **2016**, *184*, 450–463. [CrossRef]
20. Shi, K.; Chen, Y.; Yu, B.; Xu, T.; Chen, Z.; Liu, R.; Li, L.; Wu, J. Modeling spatiotemporal CO2 (carbon dioxide) emission dynamics in China from DMSP-OLS nighttime stable light data using panel data analysis. *Appl. Energy* **2016**, *168*, 523–533. [CrossRef]
21. Levin, N.; Ali, S.; Crandall, D. Utilising remote sensing and big data to quantify conflict intensity: The Arab Spring as a case study. *Appl. Geogr.* **2018**, *94*, 1–17. [CrossRef]
22. Liu, X.; Ning, X.; Wang, H.; Wang, C.; Zhang, H.; Meng, J. A Rapid and Automated Urban Boundary Extraction Method Based on Nighttime Light Data in China. *Remote Sens.* **2019**, *11*, 1126. [CrossRef]
23. Liu, Y.; Hu, Y.; Sun, H.; Zhou, G. Study on Residents' Quality of Life in the Context of Urban Shrinkage: Analysis Based on Subjective and Objective Data. *J. Urban Plan. Dev.* **2020**, *146*, 05020015. [CrossRef]
24. Zhou, Y.; Li, C.; Zheng, W.; Rong, Y.; Liu, W. Identification of urban shrinkage using NPP-VIIRS nighttime light data at the county level in China. *Cities* **2021**, *118*, 103373. [CrossRef]
25. Fu, D.; Xia, X.; Duan, M.; Zhang, X.; Li, X.; Wang, J.; Liu, J. Mapping nighttime PM2.5 from VIIRS DNB using a linear mixed-effect model. *Atmospheric Environ.* **2018**, *178*, 214–222. [CrossRef]
26. Wang, J.; Aegerter, C.; Xu, X.; Szykman, J.J. Potential application of VIIRS Day/Night Band for monitoring nighttime surface PM2. 5 air quality from space. *Atmos. Environ.* **2016**, *124*, 55–63. [CrossRef]
27. Huang, Y.; Song, Z.; Yang, H.; Yu, B.; Liu, H.; Che, T.; Chen, J.; Wu, J.; Shu, S.; Peng, X.; et al. Snow cover detection in mid-latitude mountainous and polar regions using nighttime light data. *Remote Sens. Environ.* **2021**, *268*, 112766. [CrossRef]
28. Elvidge, C.; Ghosh, T.; Hsu, F.-C.; Zhizhin, M.; Bazilian, M. The Dimming of Lights in China during the COVID-19 Pandemic. *Remote Sens.* **2020**, *12*, 2851. [CrossRef]
29. Lan, T.; Shao, G.; Tang, L.; Xu, Z.; Zhu, W.; Liu, L. Quantifying Spatiotemporal Changes in Human Activities Induced by COVID-19 Pandemic Using Daily Nighttime Light Data. *IEEE J. Sel. Top. Appl. Earth Obs. Remote Sens.* **2021**, *14*, 2740–2753. [CrossRef]
30. Huang, Q.; Yang, X.; Gao, B.; Yang, Y.; Zhao, Y. Application of DMSP/OLS nighttime light images: A meta-analysis and a systematic literature review. *Remote Sens.* **2014**, *6*, 6844–6866. [CrossRef]
31. Liao, L.B.; Weiss, S.; Mills, S.; Hauss, B. Suomi NPP VIIRS day-night band on-orbit performance. *J. Geophys. Res. Atmos.* **2013**, *118*, 12705–12718. [CrossRef]
32. Chen, H.; Xiong, X.; Link, D.O.; Sun, C.; Chiang, K. NOAA-20 Visible Infrared Imaging Radiometer Suite day–night band on-orbit calibration and performance. *J. Appl. Remote Sens.* **2020**, *14*, 034516. [CrossRef]
33. Hashitera, S.; Kohiyama, M.; Maki, N.; Fujita, H. Use of DMSP-OLS Images for Early Identification of Impacted Areas due to the 1999 Marmara Earthquake Disaster. In Proceedings of the 20th Asian Conference on Remote Sensing, Hong Kong, China, 22–25 November 1999; Volume 2.
34. Cao, C.; Shao, X.; Uprety, S. Detecting Light Outages After Severe Storms Using the S-NPP/VIIRS Day/Night Band Radiances. *IEEE Geosci. Remote Sens. Lett.* **2013**, *10*, 1582–1586. [CrossRef]
35. Cole, T.A.; Wanik, D.W.; Molthan, A.L.; Román, M.O.; Griffin, R.E. Synergistic Use of Nighttime Satellite Data, Electric Utility Infrastructure, and Ambient Population to Improve Power Outage Detections in Urban Areas. *Remote Sens.* **2017**, *9*, 286. [CrossRef]
36. Fan, X.; Nie, G.; Deng, Y.; An, J.; Zhou, J.; Li, H. Rapid detection of earthquake damage areas using VIIRS nearly constant contrast night-time light data. *Int. J. Remote Sens.* **2018**, *40*, 2386–2409. [CrossRef]
37. Sarkar, S. Rapid assessment of cyclone damage using NPP-VIIRS DNB and ancillary data. *Nat. Hazards* **2021**, *106*, 579–593. [CrossRef] [PubMed]
38. Elvidge, C.D.; Baugh, K.; Zhizhin, M.; Hsu, F.C.; Ghosh, T. VIIRS night-time lights. *Int. J. Remote Sens.* **2017**, *38*, 5860–5879. [CrossRef]
39. Wikipedia contributors. 2021 Texas Power Crisis. Wikipedia, The Free Encyclopedia. Wikipedia, The Free Encyclopedia, January 15th 2022. Web. 17 January 2022. Available online: https://en.wikipedia.org/wiki/2021 (accessed on 1 October 2022).

40. Aldhous, P.; Lee, S.; Hirji, Z. The Texas Winter Storm And Power Outages Killed Hundreds More People Than The State Says. BuzzFeed News. Available online: https://www.buzzfeednews.com/article/peteraldhous/texas-winter-storm-power-outage-death-toll. (accessed on 1 October 2022).

41. Winter Storm Uri After-Action Review: Findings Report (PDF) (Report). City of Austin & Travis County. 4 November 2021. Archived (PDF) from the original on 5 November 2021. Available online: https://www.austintexas.gov/sites/default/files/files/HSEM/2021-Winter-Storm-Uri-AAR-Findings-Report.pdf (accessed on 1 October 2022).

42. Sullivan, B.K.; Malick, N.S. 5 Million Americans Have Lost Power From Texas to North Dakota After Devastating Winter Storm. Time. Available online: https://time.com/5939633/texas-power-outage-blackouts/ (accessed on 1 October 2022).

43. Shao, X.; Cao, C.; Zhang, B.; Qiu, S.; Elvidge, C.; Von Hendy, M. Radiometric calibration of DMSP-OLS sensor using VIIRS day/night band. In *Earth Observing Missions and Sensors: Development, Implementation, and Characterization III*; SPIE: Bellingham, WA, USA, 2014.

44. Song, S.-K.; Choi, Y.-N.; Choi, Y.; Flynn, J.; Sadeghi, B. Characteristics of aerosol chemical components and their impacts on direct radiative forcing at urban and suburban locations in Southeast Texas. *Atmospheric Environ.* **2020**, *246*, 118151. [CrossRef]

45. AERONET Site Information Database. Available online: https://aeronet.gsfc.nasa.gov/new_web/photo_db_v3/Univ_of_Houston.html (accessed on 1 October 2022).

46. Platnick, S.; Meyer, K.; Wind, G.; Holz, R.E.; Amarasinghe, N.; Hubanks, P.A.; Veglio, P. The NASA MODIS-VIIRS continuity cloud optical properties products. *Remote Sens.* **2020**, *13*, 2. [CrossRef]

47. Vermote, E.F.; Vermeulen, A. Atmospheric correction algorithm: Spectral reflectances (MOD09). *ATBD Version* **1999**, *4*, 1–107.

48. Berk, A.; Anderson, G.P.; Acharya, P.K.; Bernstein, L.S.; Muratov, L.; Lee, J.; Fox, M.; Adler-Golder, S.M.; Chetwynd, J.H.; Hoke, M.L.; et al. MODTRAN 5: A reformulated atmospheric band model with auxiliary species and practical multiple scattering options: Update. In *Algorithms and Technologies for Multispectral, Hyperspectral, and Ultraspectral Imagery X*; Shen, S.S., Lewis, P.L., Eds.; International Society for Optics and Photonics: Bellingham, WA, USA, 2005; Volume 5806, pp. 662–668. ISBN 9780819457912.

49. Miller, S.D.; Turner, R.E. A Dynamic Lunar Spectral Irradiance Data Set for NPOESS/VIIRS Day/Night Band Nighttime Environmental Applications. *IEEE Trans. Geosci. Remote Sens.* **2009**, *47*, 2316–2329. [CrossRef]

50. Schueler, C.F.; Thomas, F.L.; Steven, D.M. VIIRS constant spatial-resolution advantages. *Int. J. Remote Sens.* **2013**, *34*, 5761–5777. [CrossRef]

51. Baugh, K.; Elvidge, C.D.; Ghosh, T.; Ziskin, D. Development of a 2009 Stable Lights Product using DMSP-OLS data. *Proc. Asia-Pacific Adv. Netw.* **2010**, *30*, 114. [CrossRef]

52. Yuan, X.; Jia, L.; Menenti, M.; Zhou, J.; Chen, Q. Filtering the NPP-VIIRS Nighttime Light Data for Improved Detection of Settlements in Africa. *Remote Sens.* **2019**, *11*, 3002. [CrossRef]

53. Ryan, R.E.; Pagnutti, M.; Burch, K.; Leigh, L.; Ruggles, T.; Cao, C.; Aaron, D.; Blonski, S.; Helder, D. The Terra Vega Active Light Source: A First Step in a New Approach to Perform Nighttime Absolute Radiometric Calibrations and Early Results Calibrating the VIIRS DNB. *Remote Sens.* **2019**, *11*, 710. [CrossRef]

54. Holben, B.N.; Eck, T.F.; Slutsker, I.A.; Tanre, D.; Buis, J.P.; Setzer, A.; Smirnov, A. AERONET—A federated instrument network and data archive for aerosol characterisation. *Remote Sens. Environ.* **1998**, *66*, 1–16. [CrossRef]

55. Tan, F.; Lim, H.S.; Abdullah, K.; Holben, B. Estimation of aerosol optical depth at different wavelengths by multiple regression method. *Environ. Sci. Pollut. Res.* **2015**, *23*, 2735–2748. [CrossRef]

56. Li, X.; Ma, R.; Zhang, Q.; Li, D.; Liu, S.; He, T.; Zhao, L. Anisotropic characteristic of artificial light at night–Systematic investigation with VIIRS DNB multi-temporal observations. *Remote Sens. Environ.* **2019**, *233*, 111357. [CrossRef]

57. Li, X.; Shang, X.; Zhang, Q.; Li, D.; Chen, F.; Jia, M.; Wang, Y. Using radiant intensity to characterize the anisotropy of satellite-derived city light at night. *Remote Sens. Environ.* **2022**, *271*, 112920. [CrossRef]